



## Research Paper

# Photocatalytic hydrogen production over plasmonic AuCu/CaIn<sub>2</sub>S<sub>4</sub> composites with different AuCu atomic arrangements

Jianjun Ding<sup>a,b,\*</sup>, Xiangyang Li<sup>a,b</sup>, Lin Chen<sup>a,b</sup>, Xian Zhang<sup>a,b</sup>, Xingyou Tian<sup>a,b</sup><sup>a</sup> Institute of Applied Technology, Hefei Institutes of Physical Science, Chinese Academy of Sciences, Hefei 230088, People's Republic of China<sup>b</sup> CAS Key Laboratory of Photovoltaic and Energy Conservation Materials, Chinese Academy of Sciences, Hefei 230031, People's Republic of China

## ARTICLE INFO

## Keywords:

CaIn<sub>2</sub>S<sub>4</sub>  
AuCu  
Atomic arrangement  
Photocatalytic hydrogen production  
Plasmonic photocatalysts

## ABSTRACT

Plasmonic AuCu bimetallic nanoparticles supported on monoclinic CaIn<sub>2</sub>S<sub>4</sub> have been synthesized through the photoreduction method, by which AuCu bimetallic nanoparticles with different atomic arrangements were site-selectively photo-deposited at the edges of CaIn<sub>2</sub>S<sub>4</sub> surface nanosteps. The obtained plasmonic composites were characterized by XRD, TEM, photoelectrochemical analysis, XPS, UV-vis and PL spectroscopy. The results showed that AuCu bimetallic nanoparticles with alloy structure showed better performance for light absorption, charge separation and photocatalytic activity compared to AuCu core-shell structure. Especially, alloyed Au<sub>0.4</sub>Cu<sub>0.1</sub>/CaIn<sub>2</sub>S<sub>4</sub> composite exhibited the highest visible activity for hydrogen production from Na<sub>2</sub>S/Na<sub>2</sub>SO<sub>3</sub> solution with a rate of 452.8 μmol/h, over 2.2, 10.0, 63.8 and 76.7 times higher than that of core-shell Cu<sub>0.1</sub>/Au<sub>0.4</sub>/CaIn<sub>2</sub>S<sub>4</sub>, Au<sub>0.5</sub>/CaIn<sub>2</sub>S<sub>4</sub>, Cu<sub>0.5</sub>/CaIn<sub>2</sub>S<sub>4</sub> and CaIn<sub>2</sub>S<sub>4</sub>, respectively. The enhanced photocatalytic performance of AuCu/CaIn<sub>2</sub>S<sub>4</sub> composites could be mainly ascribed to the synergistic effect in AuCu bimetallic nanoparticles and the surface plasmon resonance effect of Au.

## 1. Introduction

Semiconductor photocatalysis has been attracting worldwide attention for environmental purification and solar energy conversion, especially for photocatalytic hydrogen production, which is considered as a sustainable and clean energy to solve the environmental deterioration and energy crisis. However, weak visible absorption and low photocatalytic efficiency limit the application of the technology. To overcome these drawbacks, plasmonic photocatalyst, that is plasmonic-metal/semiconductor composite, is a promising solution for simultaneously efficient charge separation and photo absorption [1–6]. Nobel metal nanoparticles, such as Au and Ag, are widely studied due to their characteristic of localized surface plasmon resonance (SPR). The SPR wavelength can be controlled range from the visible to the near infrared by changing the metal nanoparticles' size, shape and the surrounding environment [7–10]. Under SPR excitation, metal nanoparticles as co-catalyst can efficiently harvest light energy to broaden the light absorption range and the photogenerated electrons can be transferred to the semiconductor by direct energy transfer or resonant energy transfer [11,12], which can suppress the recombination of the charge carriers and therefore enhance the photocatalytic activity.

Compared to monometallic nanoparticles, bimetallic nanoparticles show unique performance in catalysis through the synergistic effect

between the two metals [13–20]. Bimetallic structure facilitates the transfer of electrons between the two metallic parts, leading to the further improvement of electron-hole separation. Various bimetallic nanoparticles, such as AuPt [21–23], AuCu [24,25], AuPd [26,27] and AuAg [28–30], exhibited much higher photocatalytic activity for a variety of photocatalytic reactions than their corresponding monometallic counterparts. According to the arrangement of metallic atoms, bimetallic nanoparticles may be commonly classified into alloy, core-shell, subcluster segregated and three shell structures [31]. Among these bimetallic nanoparticles, AuCu bimetallic nanoparticles are particularly interested due to their excellent photocatalytic activities. For example, AuCu alloy nanoparticles exhibit enhancing photocatalytic activities for hydrogen production, CO<sub>2</sub> reduction and aerobic oxidation than Au or Cu monometallic photocatalysts [32–34]. Meanwhile, significantly improved activity under visible light was also observed by SPR effect of AuCu core-shell nanoparticles [35,36]. Although bimetallic plasmonic photocatalysts have been widely synthesized and studied in recent years, few studies have been investigated the effects of different atomic arrangements on the photocatalytic performance for hydrogen production.

In our previous work, AuPt alloy nanoparticles were site-selectively deposited at the edges of CaIn<sub>2</sub>S<sub>4</sub> nanosteps using the photoreduction method, which showed enhanced activity for photocatalytic hydrogen

\* Corresponding author at: Institute of Applied Technology, Hefei Institutes of Physical Science, Chinese Academy of Sciences, Hefei 230088, People's Republic of China.  
E-mail address: [dingjj@rntek.cas.cn](mailto:dingjj@rntek.cas.cn) (J. Ding).

production [37]. The site-selective deposition of cocatalysts has been widely proved to be beneficial for the effective separation of the photogenerated charges compared to the homogeneous deposition [38–43]. In this paper, the modification of plasmonic Au with cheap metal Cu is further studied. Both the AuCu alloy and core-shell nanoparticles were successfully deposited at the  $\text{CaIn}_2\text{S}_4$  nanosteps, respectively. As expected that the obtained  $\text{AuCu}/\text{CaIn}_2\text{S}_4$  composites exhibited remarkably enhanced activities for photocatalytic hydrogen production under visible light irradiation. Compared to core-shell AuCu nanoparticles, AuCu alloy structure was more favourable for photocatalytic hydrogen production. The effect of the atomic arrangement of AuCu bimetallic nanoparticles on photocatalytic performance of  $\text{CaIn}_2\text{S}_4$  is unambiguously confirmed.

## 2. Experimental section

### 2.1. Chemicals

All reagents were commercial and used without further purification. Indium nitrate ( $(\text{InN}_3\text{O}_9)_x\text{H}_2\text{O}$ , 99.9%) and chloroauric acid ( $(\text{HAuCl}_4\cdot 3\text{H}_2\text{O}$ , 99.9%) were purchased from Aladdin Industrial Inc. All other reagents were at least of analytical reagent grade supplied by Sinopharm Chemical Reagent Co., Ltd.

### 2.2. Synthesis of $\text{CaIn}_2\text{S}_4$

Monoclinic  $\text{CaIn}_2\text{S}_4$  was prepared using the high-temperature sulfurization method from the oxide precursor  $\text{CaIn}_2\text{O}_4$  nanorods according to our previous work [44].

### 2.3. Site-selective photo-deposition of AuCu alloy nanoparticles on $\text{CaIn}_2\text{S}_4$

A 300 W Xe arc lamp (PLS-SXE 300, Beijing Perfectlight Co., Ltd.), equipped with UV and IR cutoff filters, was used as the visible source ( $420 \text{ nm} \leq \lambda \leq 750 \text{ nm}$ ). In a typical preparation, 100 mg  $\text{CaIn}_2\text{S}_4$ , 315 mg  $\text{Na}_2\text{SO}_3$  and 600 mg  $\text{Na}_2\text{S}\cdot 9\text{H}_2\text{O}$  were dispersed into 100 mL deionized water to obtain a homogeneous suspension. Then a calculated amount of  $\text{Cu}(\text{NO}_3)_2$  and  $\text{HAuCl}_4$  was added and stirred for 30 min. Before photo-irradiated for 2 h under visible light, the suspension was purged with pure  $\text{N}_2$ . At last, the obtained powders were filtered, washed and dried at 353 K for 12 h. The loading amount of metal nanoparticles was set at 0.5 wt%. The samples with different weight ratio of Au to Cu were abbreviated as  $\text{Au}_{0.45}\text{Cu}_{0.05}/\text{CaIn}_2\text{S}_4$  (A4.5C0.5/CIS),  $\text{Au}_{0.4}\text{Cu}_{0.1}/\text{CaIn}_2\text{S}_4$  (A4C1/CIS),  $\text{Au}_{0.3}\text{Cu}_{0.2}/\text{CaIn}_2\text{S}_4$  (A3C2/CIS),  $\text{Au}_{0.2}\text{Cu}_{0.3}/\text{CaIn}_2\text{S}_4$  (A2C3/CIS) and  $\text{Au}_{0.1}\text{Cu}_{0.4}/\text{CaIn}_2\text{S}_4$  (A1C4/CIS), respectively.  $\text{Au}_{0.5}/\text{CaIn}_2\text{S}_4$  (A5/CIS) and  $\text{Cu}_{0.5}/\text{CaIn}_2\text{S}_4$  (C5/CIS) were also fabricated through a similar procedure, in the absence of  $\text{Cu}(\text{NO}_3)_2$  and  $\text{HAuCl}_4$ , respectively.

### 2.4. Site-selective photo-deposition of AuCu core-shell nanoparticles on $\text{CaIn}_2\text{S}_4$

Site-selective photo-deposition of  $\text{Cu}_{0.1}/\text{Au}_{0.4}$  core-shell nanoparticles on  $\text{CaIn}_2\text{S}_4$  was carried out via two-step photoreduction reaction. Briefly, under visible light irradiation, Au nanoparticles with a content of 0.4 wt% were firstly photo-deposited at the edges of  $\text{CaIn}_2\text{S}_4$  nanosteps to obtain  $\text{Au}_{0.4}/\text{CaIn}_2\text{S}_4$ , and then 0.1 wt% Cu was further photo-deposited on  $\text{Au}_{0.4}/\text{CaIn}_2\text{S}_4$ . The obtained product was labelled as  $\text{Cu}_{0.1}/\text{Au}_{0.4}/\text{CaIn}_2\text{S}_4$  (C1/A4/CIS). The metal content in C1/A4/CIS composite was also set at 0.5 wt%.

### 2.5. Structure characterization

Powder X-ray diffraction (XRD) patterns were collected to analysis the crystal structure on a diffractometer (Rigaku TTR III) with a  $\text{Cu K}\alpha$  radiation source. The microstructure was studied on a field-emission

transmission electron microscope (JEM-2100F). The elemental compositions were determined by inductively coupled plasma atomic emission spectrometry (ICP-AES, Optima 7300 DV, PerkinElmer Corporation). The absorption spectrum was recorded by a UV-vis spectrometer (SolidSpec 3700) in the range of  $\lambda = 200\text{--}800 \text{ nm}$ . X-ray photoelectron spectroscope (ESCALAB 250) was used to investigate the surface composition. Fluorospectro-photometer (JY Fluorolog-3-Tou) was employed to determine the photoluminescent spectra. Electrochemical data were collected using an electrochemical analyzer (CHI-760D) in a three-electrode configuration consisting of a counter electrode (Pt wire), a reference electrode ( $\text{Ag}/\text{AgCl}$ ) and a working electrode. The composite working electrodes with an active area of  $0.5 \text{ cm}^2$  were prepared using a dip-coating method.  $\text{Na}_2\text{SO}_4$  (1 mol/L, pH = 7) solution was used as the electrolyte.

### 2.6. Photocatalytic experiments

The photocatalytic activities for hydrogen production were tested using a homemade top-irradiation gas-closed circulation reactor with an outside cooling-water jacket. In a typical test, 10 mg photocatalyst, 3.15 g  $\text{Na}_2\text{SO}_3$ , 6.0 g  $\text{Na}_2\text{S}\cdot 9\text{H}_2\text{O}$  and 100 mL deionized water was firstly added into the reactor to form a homogeneous suspension under stirring. Prior to irradiation under visible light ( $420 \text{ nm} \leq \lambda \leq 750 \text{ nm}$ ), the suspension was purged with pure  $\text{N}_2$  to remove the dissolved air. During the photocatalytic reaction, 0.5 mL gas was collected intermittently and analyzed online using a gas chromatograph (Kexiao GC-1690 equipped with a TDX01 column).

To evaluate the SPR effect of Au, different band-pass filters ( $\lambda = 435, 450, 475, 500, 520, 550$  and  $600 \text{ nm}$ , half-width = 15 nm, Beijing Perfectlight Co., Ltd.) were used on the basis of UV and IR cutoff filters abovementioned.

The photocatalytic stability was performed using cycle experiment. The photocatalyst after the photocatalytic reaction was collected, washed and reused in the fresh  $\text{Na}_2\text{S}/\text{Na}_2\text{SO}_3$  solution for the next round.

## 3. Results and discussion

### 3.1. Characterization of $\text{AuCu}/\text{CaIn}_2\text{S}_4$ composites

**Fig. 1** shows the XRD patterns of the prepared photocatalysts of A5/CIS, C5/CIS, A4C1/CIS, C1/A4/CIS and pure  $\text{CaIn}_2\text{S}_4$ . After the deposition of metal nanoparticles, the XRD patterns for all composites did not change including XRD peaks' position and intensity. The diffraction peaks for all samples can be ascribed to the phase of monoclinic  $\text{CaIn}_2\text{S}_4$ , indicating that the crystal structure of  $\text{CaIn}_2\text{S}_4$  kept stable

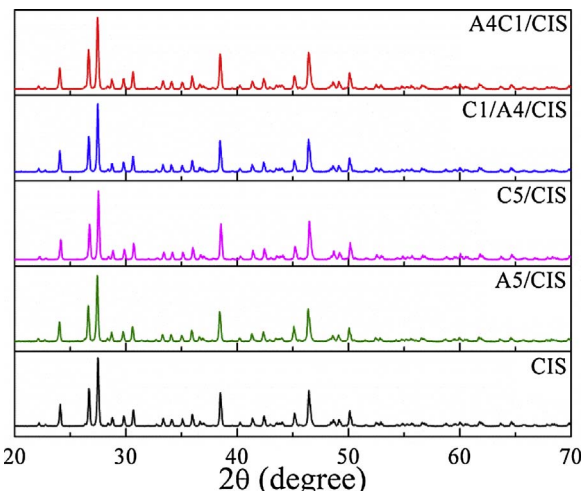


**Fig. 1.** XRD patterns of CIS, A5/CIS, C5/CIS, C1/A4/CIS and A4C1/CIS photocatalysts.

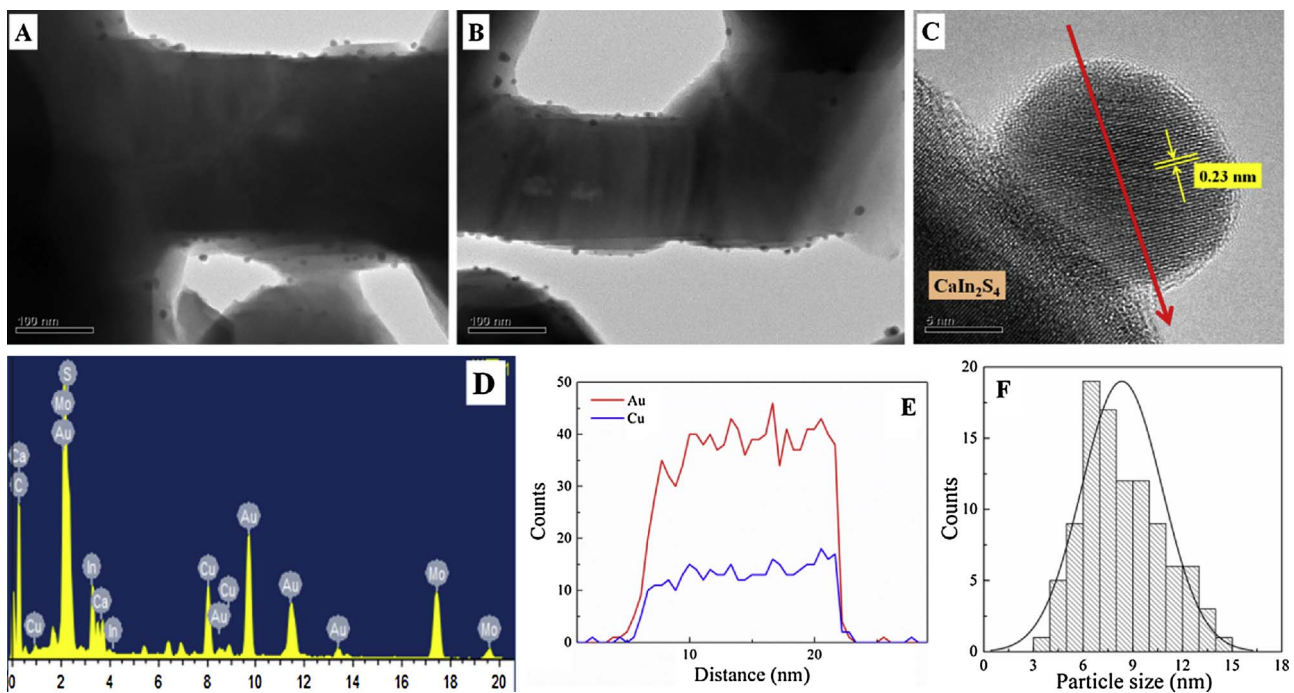


Fig. 2. TEM images and size distribution of A4C1/CIS composite.

during the photo-reduction of metal precursors to metal nanoparticles in the suspension. No characteristic diffraction peaks of Au or Cu can be observed or distinguished from the enlarged view of XRD patterns due to the low content, small size and high dispersion of the metal nanoparticles.

To confirm the successful deposition of AuCu bimetallic nanoparticles with different atomic arrangements on the  $\text{CaIn}_2\text{S}_4$  nanosteps, microstructure analysis was employed by TEM characterization. It's well known that the photocatalytic reaction sites are effectively separated at the nanostep structure because the photogenerated electrons and holes can readily migrate to the edges and grooves to serve as the reduction and oxidation reaction sites, respectively [45–48]. In this case, the metal precursors, including  $\text{Cu}(\text{NO}_3)_2$  and  $\text{HAuCl}_4$ , can be *in-situ* photoreduced to metal nanoparticles by the accumulated electrons at the edge sites. From Fig. 2A and B, the obtained metal nanoparticles were all site-selectively deposited at the edges of  $\text{CaIn}_2\text{S}_4$  nanosteps, indicating the photogenerated electrons were readily available for the reduction reaction at the nanostep's edges. The spacing lattice of the fringe is calculated to be 0.23 nm from the high-resolution image (Fig. 2C), which is between the value of standard Au ( $a = 0.2355$  nm) and Cu ( $a = 0.2087$  nm), and is in agreement with the Vegard's law ( $a_{\text{alloy}} = 0.2355 \times 0.8 + 0.2087 \times 0.2 = 0.2301$  nm) [49]. The corresponding EDS spectrum (Fig. 2D) demonstrated that both Au and Cu elements existed in the selective nanoparticle. This was further confirmed by the line scanning profiles (Fig. 2E), where Au and Cu components were mixed homogeneously to successfully form an alloy structure. The content of Au and Cu was found to be 0.392% and 0.094% from the ICP-AES analysis, respectively. The average diameter of AuCu alloy nanoparticles was about 8.3 nm (Fig. 2D), which is much lower than that of Au nanoparticles in A5/CIS composite (18.3 nm) [37], which could be ascribed to the strong metal-support interaction between Cu and  $\text{CaIn}_2\text{S}_4$ . For alloyed AuCu/ $\text{CaIn}_2\text{S}_4$  composites, the introduction of Cu component to form AuCu alloy structure can increase the interaction intensity between metal and  $\text{CaIn}_2\text{S}_4$ , resulting the decrease of the mean diameter [50,51].

Fig. 3 shows typical TEM images for C1/A4/CIS composite. Similar to A4C1/CIS composite, metal nanoparticles were also site-selectively deposited at the edges of  $\text{CaIn}_2\text{S}_4$  nanosteps. According to the synthetic

strategy, when the  $\text{Au}_{0.4}/\text{CaIn}_2\text{S}_4$  composite is irradiated under visible light, both Au and  $\text{CaIn}_2\text{S}_4$  can generate electrons. As the Fermi level of Au is more oxidizing than the conduction band of  $\text{CaIn}_2\text{S}_4$ , the photo-generated electrons in the conduction band of  $\text{CaIn}_2\text{S}_4$  can easily transfer to the sites of Au. Therefore,  $\text{Cu}(\text{NO}_3)_2$  can be *in-situ* photoreduced to Cu nanoparticles on the surface of Au to form core-shell structure. From Fig. 3C, Cu nanoparticles with a lattice spacing of 0.21 nm were detected and located on the Au surface of  $\text{Au}_{0.4}/\text{CaIn}_2\text{S}_4$  to form a core(Au)-shell(Cu) structure. Correspondingly, the EDS spectrum showed the characteristic signal of both Au and Cu metals. By STEM-EDS line scans, the presence of the Cu shell and Au core was clearly confirmed. The results proved that AuCu core-shell nanoparticles were also successfully synthesized and site-selectively deposited at the edges of  $\text{CaIn}_2\text{S}_4$  nanosteps after the two-step photo-reduction reaction. The content of Au and Cu was 0.374% and 0.089%, respectively, which was almost the same to that of A4C1/CIS composite. Because Cu nanoparticles were directly supported on the surface of Au nanoparticles, the mean diameter of AuCu core-shell nanoparticles was slightly increased to 20.1 nm (Fig. 3D). TEM results clearly prove that AuCu bimetallic nanoparticles with different atomic arrangements site-selectively photo-deposited at the edge of  $\text{CaIn}_2\text{S}_4$  nanosteps.

The UV-vis absorption spectra of AuCu/ $\text{CaIn}_2\text{S}_4$  composites, together with that of  $\text{CaIn}_2\text{S}_4$ , were investigated and shown in Fig. 4.  $\text{CaIn}_2\text{S}_4$  has absorption from the UV range up to about 450 nm. The steep absorption edge indicates that the visible absorption is ascribed to the bandgap transition. The direct band gap was estimated to be 2.6 eV. After the deposition of Au nanoparticles, A5/CIS composite shows clear visible absorption beyond the absorption region of  $\text{CaIn}_2\text{S}_4$ , which is assigned to the SPR absorption of Au nanoparticles supported on  $\text{CaIn}_2\text{S}_4$  [52]. The absorption for C5/CIS composite in visible region is very weak which could be caused by the scattering effect rather than the SPR effect of Cu nanoparticles [53,54]. As shown in Fig. 4, AuCu bimetallic nanoparticles with different atomic arrangements exhibit different absorption characteristics. For alloyed A4C1/CIS composite, the addition of Cu to form AuCu alloy structure weaken the visible absorption and SPR peak of Au blue-shifts to a shorter wavelength due to the decrease of Au nanoparticles in size and in content, while the absorption curve of C1/A4/CIS composite is similar to that of C5/CIS

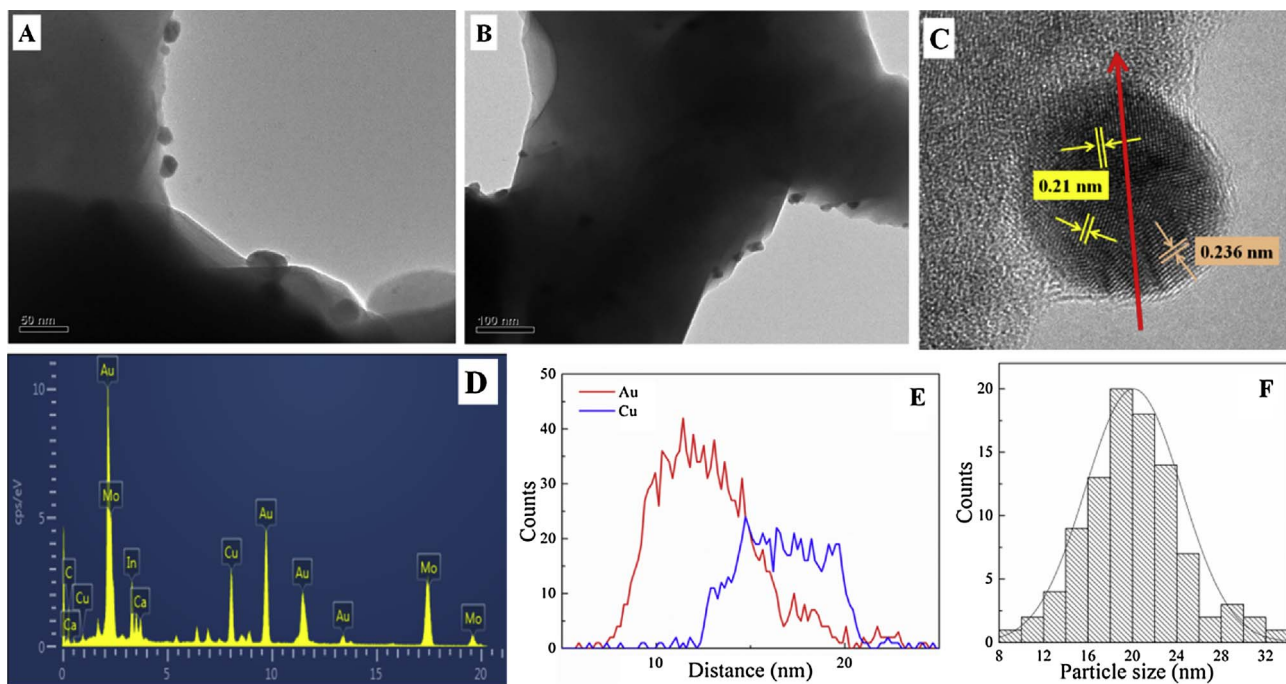


Fig. 3. TEM images and size distribution of C1/A4/CIS composite.

composite. The main reason for the disappearance of Au SPR band in C1/A4/CIS composite is that the Au core is covered by Cu shell and the optical contribution from Au core is decreased largely [30]. The result indicates that AuCu alloy structure is more favourable for the effective absorption of visible light compare to AuCu core-shell structure.

In order to investigate the compositions and electronic structure of surface atoms of AuCu bimetallic nanoparticles on  $\text{CaIn}_2\text{S}_4$  surface,

high-resolution XPS spectra of both Au 4f and Cu 2p were measured and shown in Fig. 5. The two peaks located at 83.6 and 87.3 eV are the signals of  $\text{Au } 4\text{f}_{7/2}$  and  $4\text{f}_{5/2}$  of  $\text{Au}^0$  species in A5/CIS composite [55], while the binding energies of 932.4 and 952.2 eV are characteristic of metallic copper in C5/CIS composite [56]. There is almost no oxidized species of Au or Cu observed because the photoreduction reaction was carried out under the protection of nitrogen. It's well known that

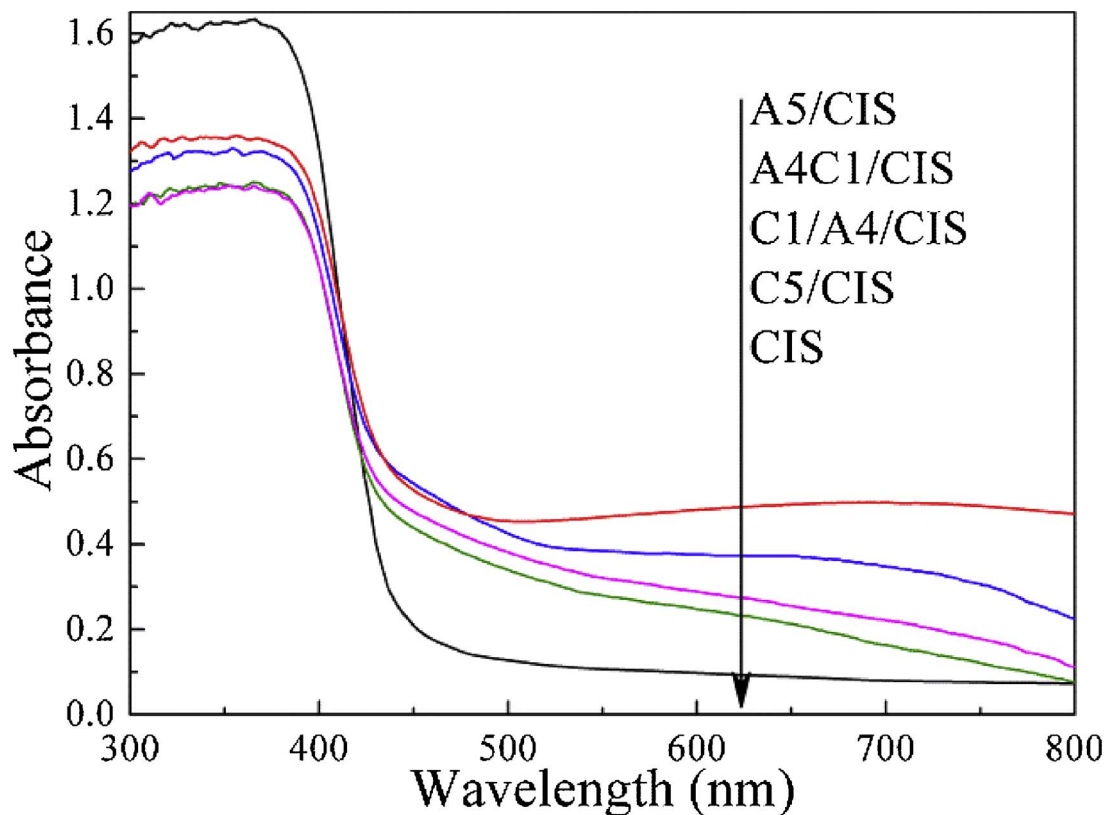


Fig. 4. UV-vis absorption spectra of CIS, A5/CIS, C5/CIS, C1/A4/CIS and A4C1/CIS photocatalysts.

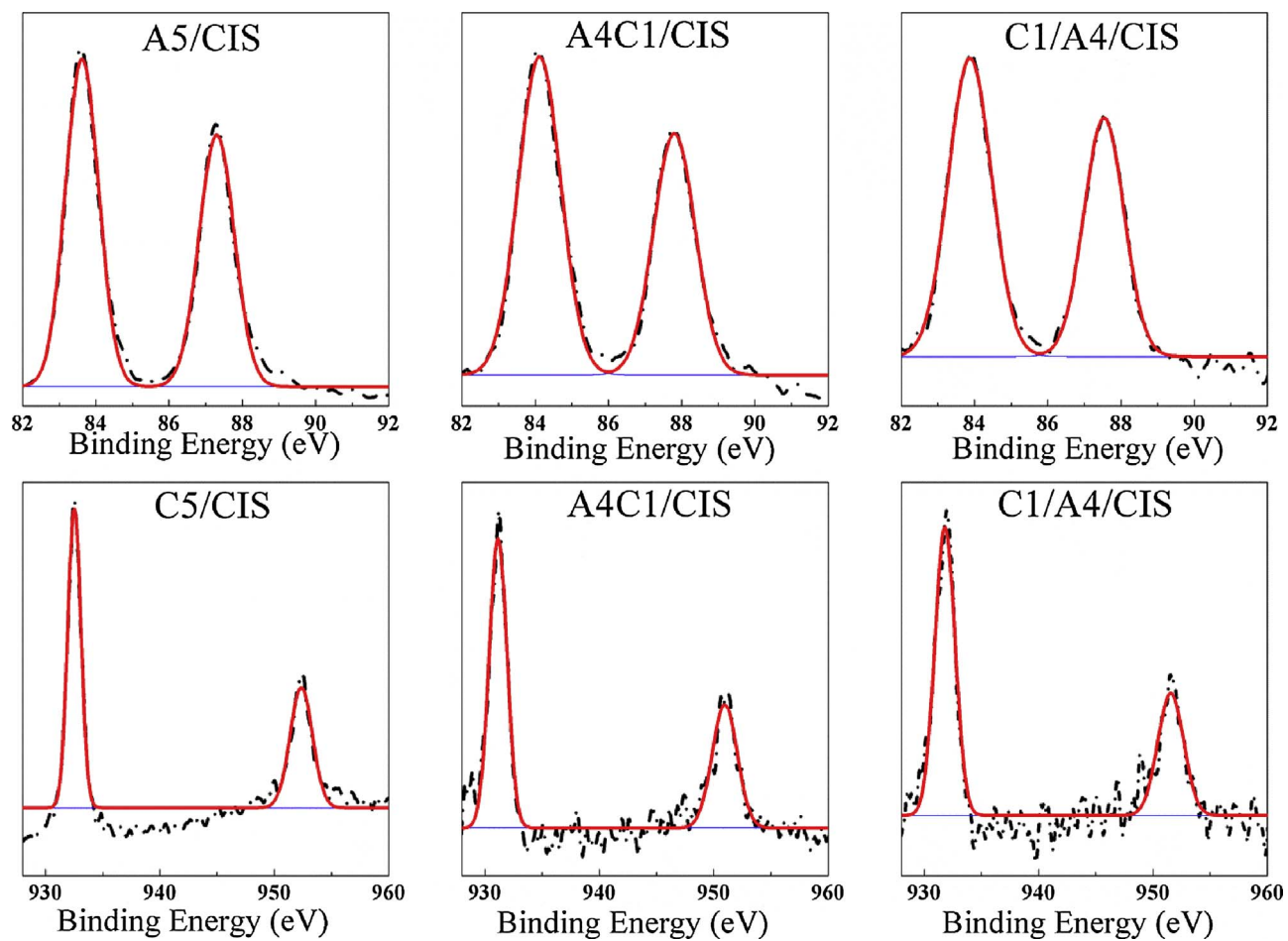


Fig. 5. XPS core level spectra of Au 4f and Cu 2p for A5/CIS, C5/CIS, C1/A4/CIS and A4C1/CIS composites.

coinage Cu is rarely used alone as plasmonic metal in plasmonic photocatalysts due to the easy oxidation of Cu [32]. In this study, the site-selective deposition of Cu at the edges of  $\text{CaIn}_2\text{S}_4$  nanosteps can make the photogenerated electrons and holes separated spatially, in which the oxidation of Cu was effectively inhibited. This demonstrates Au and Cu nanoparticles were successfully photoreduced from the metal precursors and deposited on the surface of  $\text{CaIn}_2\text{S}_4$ . The binding energies of Au 4f or Cu 2p were a little lower than that of bulk metallic Au or Cu, which might be explained by the interaction with the  $\text{CaIn}_2\text{S}_4$  substrate [57]. When AuCu/ $\text{CaIn}_2\text{S}_4$  composites were irradiated under visible light, the accumulated hot electrons generated on the sites of Au will finally transfer to the sites of Cu due to the charge re-equilibrium though the work function of Cu is lower than that of Au [58]. As a result, the binding energies of Au 4f are shifted to higher value while the peaks of Cu 2p exhibit negative shift to lower energy in both A4C1/CIS and C1/A4/CIS composites [37,59]. It should be noted that the binding energies of Au 4f (or Cu 2p) in A4C1/CIS composite were higher (or lower) than those in C1/A4/CIS composite, which means that more hot electrons transfer from Au to Cu in A4C1/CIS composite. Therefore, the formation of AuCu alloy structure is also beneficial for electron migration from Au to Cu and thus improves the separation efficiency of the photogenerated charges in alloyed AuCu/ $\text{CaIn}_2\text{S}_4$  composites, compared to AuCu core-shell structure. This hypothesis is confirmed by the following experiments of photocatalytic hydrogen production over the AuCu/ $\text{CaIn}_2\text{S}_4$  composites under visible light irradiation.

### 3.2. Photocatalytic performance of AuCu/ $\text{CaIn}_2\text{S}_4$ composites

Photocatalytic experiments for hydrogen production over the prepared photocatalysts were characterized from  $\text{Na}_2\text{S}/\text{Na}_2\text{SO}_3$  solution under visible light irradiation. No hydrogen production without the photocatalyst or light irradiation was detected, indicating that hydrogen was only produced through the photocatalytic reaction. In our previous work,  $\text{CaIn}_2\text{S}_4$  exhibited visible activity with a rate of  $5.9 \mu\text{mol}/\text{h}$  from  $\text{Na}_2\text{S}/\text{Na}_2\text{SO}_3$  solution. With the site-selective deposition of AuPt alloy, the visible hydrogen production rate was further increased to  $107.6 \mu\text{mol}/\text{h}$  (or  $10.76 \text{ mmol}/\text{h g}^{-1}$ ) for  $\text{Au}_{0.3}\text{Pt}_{0.2}/\text{CaIn}_2\text{S}_4$  composite. [37]. From Fig. 6, hydrogen production rates of all photocatalysts exhibited a linear relationship with irradiation time. The hydrogen production activity of C5/CIS composite was about  $7.1 \mu\text{mol}/\text{h}$ , lower than that of A5/CIS composite ( $45.4 \mu\text{mol}/\text{h}$ ) owing to the SPR effect of Au nanoparticles. It can be seen that the site-selective deposition of AuCu bimetallic nanoparticles can remarkably improve the hydrogen evolution of  $\text{CaIn}_2\text{S}_4$ . The synergistic photocatalytic effect between Au and Cu can provide effective charge transfer between Au and Cu in the AuCu bimetallic nanoparticles [60]. When AuCu/ $\text{CaIn}_2\text{S}_4$  composites are irradiated under visible light, the photogenerated electrons can be easily transferred from the conduction band of  $\text{CaIn}_2\text{S}_4$  to the AuCu bimetallic nanoparticles where they participate in  $\text{H}_2$  production. For C1/A4/CIS composite, the hydrogen evolution rate can reach  $205.7 \mu\text{mol}/\text{h}$  (or  $20.57 \text{ mmol}/\text{h g}^{-1}$ ) when Au and Cu exist as core-shell structure, which is 4.5, 29 and 34.9 times higher than that of A5/CIS, C5/CIS and  $\text{CaIn}_2\text{S}_4$ , respectively. To our surprise, the formation of AuCu alloy structure can further improve the hydrogen evolution activity of  $\text{CaIn}_2\text{S}_4$  to  $452.8 \mu\text{mol}/\text{h}$  (or  $45.28 \text{ mmol}/\text{h g}^{-1}$ ). The

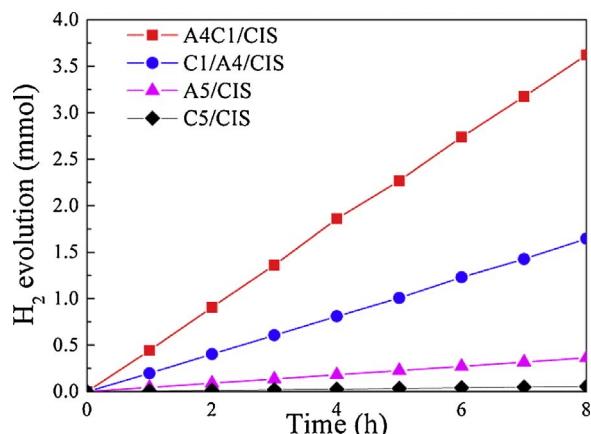


Fig. 6. Photocatalytic hydrogen production for A5/CIS, C5/CIS, C1/A4/CIS and A4C1/CIS composites under visible light irradiation.

activity of A4C1/CIS composite is 2.2 times higher than that of C1/A4/CIS composite, which indicates that the alloy structure of AuCu bimetallic nanoparticles is more beneficial for the enhancement of the hydrogen production compared to the AuCu core-shell structure. Moreover, the addition of cheap Cu to form AuCu alloy was better than that of AuPt alloy in the improvement of photocatalytic hydrogen production of  $\text{CaIn}_2\text{S}_4$  under visible light.

It's well known that the SPR effect of metal nanoparticles can improve the photocatalytic hydrogen activity for plasmonic photocatalysts. To evaluate the SPR effect of Au nanoparticles, Fig. 7 plots the hydrogen production rate obtained from C1/A4/CIS and A4C1/CIS composites as a function of the irradiation wavelength. According to previous reports, photocatalytic activity decreases with increasing the irradiation wavelength [61–63]. However, the photocatalytic activities over the AuCu/ $\text{CaIn}_2\text{S}_4$  composites experienced an initial decrease followed by a rapid increase when the incident light wavelength was 475 nm. The corresponding hydrogen production rate is 100.6 and 51.5  $\mu\text{mol}/\text{h}$  for the A4C1/CIS and C1/A4/CIS composites, respectively. Further increasing the incident light wavelength, the activity of the composites decreased, but they still could generate hydrogen from water. Since the photo irradiation was beyond the band-edge absorption of  $\text{CaIn}_2\text{S}_4$  and originated only from Au, the obtained activity for these two AuCu/ $\text{CaIn}_2\text{S}_4$  composites should be attributed to the SPR effect of Au nanoparticles, indicating the SPR effect of Au plays an important role in the enhancement of photocatalytic activity. When AuCu/ $\text{CaIn}_2\text{S}_4$  composites are irradiated under SPR excitation, the accumulated hot electrons can transfer from the sites of Au to the sites of

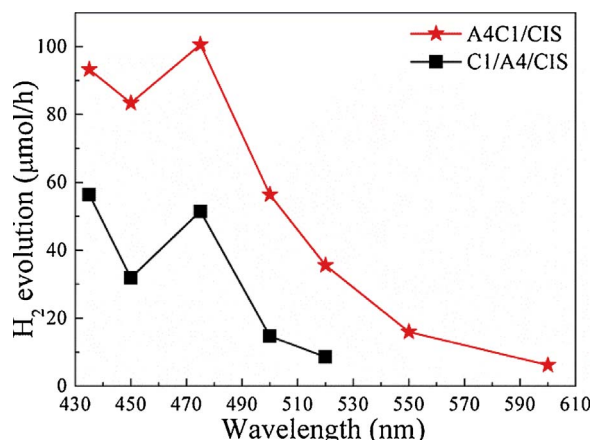


Fig. 7. Photocatalytic hydrogen production rate over C1/A4/CIS and A4C1/CIS composites as a function of the incident light wavelength. Light Source: 300 W Xe lamp + UV and IR cutoff filters + various band-pass filters.

Cu or to the conduction band of  $\text{CaIn}_2\text{S}_4$  [64], facilitating hydrogen production from water. Interesting, the longest wavelength that could be utilized for hydrogen production was about 600 and 520 nm for the A4C1/CIS and C1/A4/CIS composites, respectively. The difference in the maximum response wavelength is related to the atomic arrangement of Cu in AuCu bimetal. The SPR effect of Au core in AuCu core-shell structure was largely screened by the Cu shell and thus the maximum response wavelength was shorter in C1/A4/CIS composite than that in A4C1/CIS composite. The result demonstrates that the SPR effect of Au in AuCu bimetallic nanoparticles was beneficial for the enhancement of photocatalytic hydrogen production and strongly correlated with the atomic arrangement of AuCu bimetallic components.

Fig. 8 shows the hydrogen production rate of alloyed  $\text{Au}_{0.5-x}\text{Cu}_x/\text{CIS}$  composites with different weight ratios of Au to Cu under visible light irradiation. In the presence of a small amount of Cu, the hydrogen production rate of the  $\text{Au}_{4.5}\text{Cu}_{0.5}/\text{CIS}$  composite was greatly enhanced to 234.3  $\mu\text{mol}/\text{h}$ . The hydrogen production rate reached a maximum of 452.8  $\mu\text{mol}/\text{h}$  when the content of Cu was increased to 0.1 wt% (that is A4C1/CIS composite). With further increasing the content of Cu, however, the hydrogen production rate was decreased. In this case, the SPR-mediated enhancement of Au nanoparticles is suppressed due to the decrease in Au content. This results in decreased efficiency for both light absorption and charge separation, and decreases photocatalytic activity for hydrogen production. The stability test for 32 h over A4C1/CIS composite exhibited steady hydrogen production after four runs (Fig. 8) and the crystal structure did not change after the reaction, demonstrating the stability of the A4C1/CIS composite in the photocatalytic hydrogen production under visible light irradiation.

The significant enhancement of photocatalytic hydrogen production over the AuCu/ $\text{CaIn}_2\text{S}_4$  composites can be mainly attributed to synergistic effect of AuCu bimetal nanoparticles and the SPR effect of Au component. The site-selective deposition of AuCu bimetallic nanoparticles at the edges of  $\text{CaIn}_2\text{S}_4$  nanosteps serves as the reduction sites in the photocatalytic reaction, while the oxidation reactions take place at the grooves sites of  $\text{CaIn}_2\text{S}_4$  nanosteps. Compared to  $\text{CaIn}_2\text{S}_4$ , the spatial separation of the oxidation and reduction sites can accelerate the transfer of the photogenerated electrons from the conduction band of  $\text{CaIn}_2\text{S}_4$  to AuCu bimetallic nanoparticles. Under visible light irradiation, the accumulated electrons on the sites of Au will eventually transfer to the sites of Cu, leading to the electron density enrichment of Cu and therefore further improve the separation efficiency of the photogenerated charges. The addition of Cu to form AuCu bimetallic nanoparticles can also strengthen the metal-support interaction and promote the desorption of hydrogen molecules from the surface sites [50,51]. As a result, the site-selective deposition of AuCu bimetallic nanoparticles can significantly improve photocatalytic performance of  $\text{CaIn}_2\text{S}_4$  compared to A5/CIS and C5/CIS monometallic composites. On the other hand, the SPR effect of Au nanoparticles can absorb more visible light beyond the absorption of  $\text{CaIn}_2\text{S}_4$  and provide more electrons to participate the photocatalytic reaction. However, from Figs. 6 and 7, the enhancement of AuCu alloy nanoparticles is better than that of AuCu core-shell structure. In order to understand the mechanism of the different photocatalytic performance of these two AuCu/ $\text{CaIn}_2\text{S}_4$  composites, the information such as the efficiency of charge carriers migration and recombination, should be analyzed.

Fig. 9 shows the photoluminescent spectra of  $\text{CaIn}_2\text{S}_4$  and AuCu/ $\text{CaIn}_2\text{S}_4$  composites. The excitation wavelength is 420 nm.  $\text{CaIn}_2\text{S}_4$  exhibited two broad and strong peaks in the range of 450–800 nm. The intensity of emission peaks was in the order of  $\text{CaIn}_2\text{S}_4 > \text{C5/CIS} > \text{A5/CIS} > \text{C1/A4/CIS} > \text{A4C1/CIS}$ . As we know, the photoluminescent intensity can be usually used to reveal the separation efficiency of the photogenerated charges. Emission peak with lower intensity implies higher separation efficiency [65,66]. Therefore, the separation efficiency was in the order of  $\text{CaIn}_2\text{S}_4 < \text{C5/CIS} < \text{A5/CIS} < \text{C1/A4/CIS} < \text{A4C1/CIS}$ . The result demonstrates that the site-selective deposition of AuCu bimetallic nanoparticles is helpful to

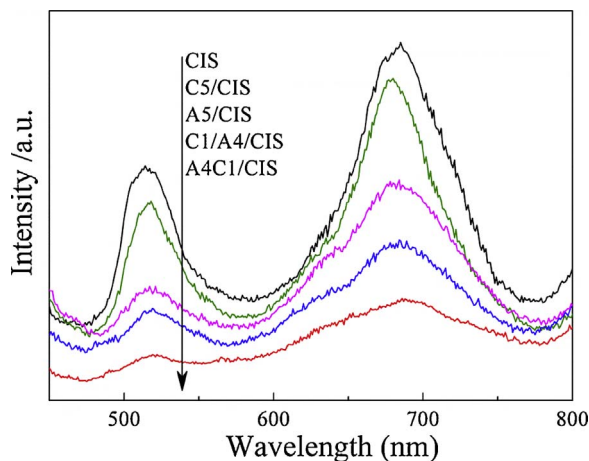
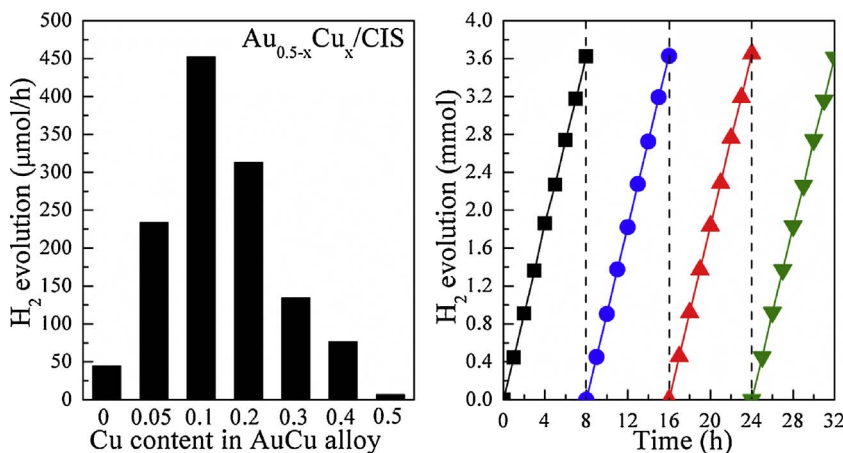


Fig. 9. Photoluminescent spectra of CIS, A5/CIS, C5/CIS, C1/A4/CIS and A4C1/CIS photocatalysts with the excitation wavelength of 420 nm.

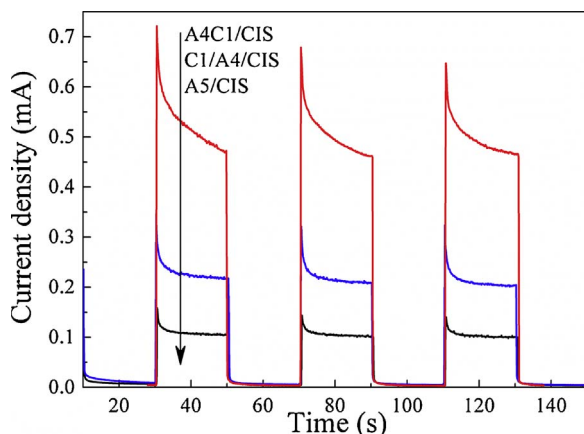


Fig. 10. Transient photocurrent density responses of A5/CIS, A4C1/CIS and C1/A4/CIS composites with light on/off cycles under visible light irradiation.

improve the transfer characteristic of the photogenerated charges compared to Au or Cu monometallic nanoparticles and the separation efficiency of AuCu alloy structure is more effective than that of AuCu core-shell structure, which is consistent with photocatalytic activity for hydrogen production. Further evidence was obtained by photoelectrochemical tests to study the charge migration property [67]. The photocurrent transient responses of the as-prepared photocatalysts were measured under visible light irradiation. As shown in Fig. 10, the photocurrent density was detected to be 0.47, 0.22 and 0.1 mA (per

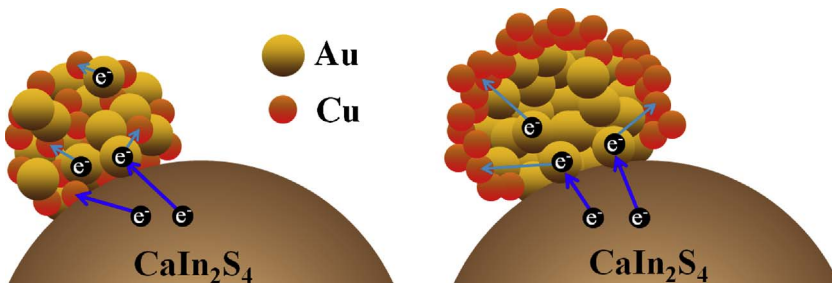
Fig. 8. The hydrogen production rate of  $\text{Au}_{0.5-x}\text{Cu}_x/\text{CIS}$  composites with different contents of Cu and the photocatalytic stability of A4C1/CIS composite under visible light irradiation.

$0.5 \text{ cm}^2$ ) for A4C1/CIS, C1/A4/CIS and A5/CIS composite, respectively, demonstrating again that alloyed A4C1/CIS composite possessed much higher charge transfer efficiency than C1/A4/CIS core-shell bimetallic composite and A5/CIS monometallic composite.

According to the above-mentioned results, the atomic arrangement of Cu in AuCu bimetallic nanoparticles plays a key role in light absorption, charge separation and photocatalytic hydrogen production. A mechanism for charge separation over the AuCu/  $\text{CaIn}_2\text{S}_4$  composites is proposed in Fig. 11. When alloyed A4C1/CIS composite is irradiated under visible light, the electrons can be transferred from the conduction band of  $\text{CaIn}_2\text{S}_4$  to the sites of Au or Cu. Meanwhile, the accumulated electrons on the sites of Au can be easily transferred to the adjacent Cu nanoparticles. Accordingly, the separation of the photogenerated charges is very effective. Electrons at the conduction band of  $\text{CaIn}_2\text{S}_4$  inhibit the reverse transportation of the electrons from the excited Au to  $\text{CaIn}_2\text{S}_4$ , but transfer to the electronic states of Au. While for C1/A4/CIS core-shell composite, Au nanoparticles were firstly site-selective deposited at the edges of  $\text{CaIn}_2\text{S}_4$  nanosteps and then Cu nanoparticles were deposited on the surface of Au to form core-shell structure. In this case, the photogenerated electrons on the conduction band of  $\text{CaIn}_2\text{S}_4$  will firstly transfer to the sites of Au, and their distance to further migrate to the shell of Cu, where they can react with water to produce hydrogen, is prolonged, compared to AuCu alloy structure. That's why the separation efficiency of AuCu core-shell structure was much lower than that of AuCu alloy nanoparticles. Moreover, the existence of Cu shell in AuCu core-shell nanoparticles may decrease the visible absorption of Au core because the incident light can be scattered by Cu shell. Therefore, the site-selective deposition of AuCu alloy nanoparticles on  $\text{CaIn}_2\text{S}_4$  nanosteps exhibits higher photocatalytic activity for hydrogen production under visible light irradiation than that of AuCu core-shell structure.

#### 4. Conclusions

In summary, we have successfully synthesized plasmonic AuCu/  $\text{CaIn}_2\text{S}_4$  composites with different AuCu atomic arrangements for the first time through the photoreduction method. During the photoreduction reaction, the metal precursors were *in-situ* photoreduced to AuCu bimetallic nanoparticles and site-selectively deposited at the edges of  $\text{CaIn}_2\text{S}_4$  nanosteps. In this case, photocatalytic reduction reaction took place at the AuCu bimetallic nanoparticles, while the grooves of  $\text{CaIn}_2\text{S}_4$  nanosteps served as photocatalytic oxidation sites. The spatial separation of photocatalytic reduction and oxidation sites was helpful for the effective separation of the photogenerated charges and therefore the deposition of AuCu bimetallic nanoparticles greatly enhanced the photocatalytic performance of  $\text{CaIn}_2\text{S}_4$ . The enhancement of photocatalytic hydrogen production from  $\text{Na}_2\text{S}/\text{Na}_2\text{SO}_3$  solution was dependent on the structure of AuCu bimetallic nanoparticles. The



results indicated that AuCu alloy nanoparticles were more beneficial for light absorption, charge separation and hydrogen production compared to AuCu core-shell structure. As a result, alloyed A4C1/CIS composite exhibited the highest activity with hydrogen production rate of 452.8  $\mu\text{mol}/\text{h}$ , which was 2.2, 10.0, 63.8 and 76.7 times higher than that of core-shell C1/A4/CIS, A5/CIS, C5/CIS and  $\text{CaIn}_2\text{S}_4$ , respectively. Moreover, the photocatalytic performance of AuCu/ $\text{CaIn}_2\text{S}_4$  composites was relevant to the wavelength of the incident light, indicating that the SPR effect of Au played an important role in the enhanced activity.

## Acknowledgements

This work was financially supported by the CASHIPS Director's Fund (YZJJ201523), Anhui Provincial Natural Science Foundation (1708085MB46) and National Natural Science Foundation of China (51303182 and 21204090).

## References

- [1] Y. Tian, T. Tatsuma, *J. Am. Chem. Soc.* 127 (2005) 7632–7637.
- [2] K. Awazu, M. Fujimaki, C. Rockstuhl, J. Tominaga, H. Murakami, Y. Ohki, N. Yoshida, T. Watanabe, *J. Am. Chem. Soc.* 130 (2008) 1676–1680.
- [3] Z.W. Liu, W.B. Hou, P. Pavaskar, M. Aykol, S.B. Cronin, *Nano Lett.* 11 (2011) 1111–1116.
- [4] S. Linic, P. Christopher, D.B. Ingram, *Nat. Mater.* 10 (2011) 911–921.
- [5] P. Wang, B.B. Huang, Y. Dai, M.H. Whangbo, *Phys. Chem. Chem. Phys.* 14 (2012) 9813–9825.
- [6] J.T. Li, S.K. Cushing, F.K. Meng, T.R. Senty, A.D. Bristow, N.Q. Wu, *Nat. Photon.* 9 (2015) 601–607.
- [7] K.L. Kelly, E. Coronado, L.L. Zhao, G.C. Schatz, *J. Phys. Chem. B* 107 (2003) 668–677.
- [8] J.J. Mock, M. Barbic, D.R. Smith, D.A. Schultz, S. Schultz, *J. Chem. Phys.* 116 (2002) 6755–6759.
- [9] A. Manjavacas, J.G. Liu, V. Kulkarni, P. Nordlander, *ACS Nano* 8 (2014) 7630–7638.
- [10] K. Qian, B.C. Sweeny, A.C. Johnston-Peck, W. Niu, J.O. Graham, J.S. DuChene, J. Qiu, Y.C. Wang, M.H. Engelhard, D. Su, E.A. Stach, W.D. Wei, *J. Am. Chem. Soc.* 136 (2014) 9842–9845.
- [11] Y. Tian, T. Tatsuma, *Chem. Commun.* 16 (2004) 1810–1811.
- [12] S.K. Cushing, J. Li, F. Meng, T.R. Senty, S. Suri, M. Zhi, M. Li, A.D. Bristow, N.Q. Wu, *J. Am. Chem. Soc.* 134 (2012) 15033–15041.
- [13] A.Q. Wang, C.M. Chang, C.Y. Mou, *J. Phys. Chem. B* 109 (2005) 18860–18867.
- [14] K. Takanabe, K. Nagaoka, K. Narai, K.I. Aika, *J. Catal.* 232 (2005) 268–275.
- [15] V.R. Stamenkovic, B.S. Mun, M. Arenz, K.J.J. Mayrhofer, C.A. Lucas, G.F. Wang, P.N. Ross, N.M. Markovic, *Nat. Mater.* 6 (2007) 241–247.
- [16] C. Chen, Y.J. Kang, Z.Y. Huo, Z.W. Zhu, W.Y. Huang, H.L. Xin, J.D. Snyder, D.G. Li, J.A. Herron, M. Mavrikakis, M.F. Chi, K.L. More, Y.D. Li, N.M. Markovic, G.A. Somorjai, P.D. Yang, V.R. Stamenkovic, *Science* 343 (2014) 1339–1343.
- [17] Y. Wang, H. Arandiyen, J. Scott, M. Akia, H.X. Dai, J.G. Deng, K.F. Aguey-Zinsou, R. Amal, *ACS Catal.* 6 (2016) 6935–6947.
- [18] S.H. Xie, Y.X. Liu, J.G. Deng, X.T. Zhao, J. Yang, K.F. Zhang, Z. Han, H. Arandiyen, H.X. Dai, *Appl. Catal. B Environ.* 206 (2017) 221–232.
- [19] X.Y. Li, Y.X. Liu, J.G. Deng, S.H. Xie, X.T. Zhao, Y. Zhang, K.F. Zhang, H. Arandiyen, G.S. Guo, H.X. Dai, *Appl. Surf. Sci.* 403 (2017) 590–600.
- [20] S.H. Xie, Y.X. Liu, J.G. Deng, S.M. Zang, Z.H. Zhang, H. Arandiyen, H.X. Dai, *Environ. Sci. Technol.* 51 (2017) 2271–2279.
- [21] F.L. Wang, Y.J. Jiang, D.J. Lawes, G.E. Ball, C.F. Zhou, Z.W. Liu, R. Amal, *ACS Catal.* 5 (2015) 3924–3931.
- [22] Z. Lou, M. Fujisuka, T. Majima, *ACS Nano* 10 (2016) 6299–6305.
- [23] S.F. Hung, Y.C. Yu, N.T. Suen, G.Q. Tzeng, C.W. Tung, Y.Y. Hsu, C.S. Hsu, C.K. Chang, T.S. Chan, H.S. Sheu, J.F. Lee, H.M. Chen, *Chem. Commun.* 52 (2016) 1567–1570.
- [24] S. Neatu, J.A. Macia-Agullo, P. Concepcion, H. Garcia, *J. Am. Chem. Soc.* 136 (2014) 15969–15976.
- [25] E. Bonmati, A. Gcsanovas, I. Angurell, J. Llorca, *Top. Catal.* 58 (2015) 77–84.
- [26] Z. Zhang, S.W. Cao, Y. Liao, C. Xue, *Appl. Catal. B Environ.* 162 (2015) 204–209.
- [27] P. Liu, X. Gu, H. Zhang, J. Cheng, J. Song, S. Su, *Appl. Catal. B Environ.* 204 (2017) 497–504.
- [28] N. Zhou, L. Polavarapu, N. Gao, Y. Pan, P. Yuan, Q. Wang, Q.H. Xu, *Nanoscale* 5 (2013) 4236–4241.
- [29] M. Tahir, B. Tahir, N.A.S. Amin, *Appl. Catal. B Environ.* 204 (2017) 548–560.
- [30] S. Kamimura, S. Yamashita, S. Abe, T. Tsubota, T. Ohno, *Appl. Catal. B Environ.* 211 (2017) 11–17.
- [31] R. Ferrando, J. Jellinek, R.L. Johnston, *Chem. Rev.* 108 (2008) 845–910.
- [32] M.Y. Liu, W. Zhou, T. Wang, D.F. Wang, L.Q. Liu, J.H. Ye, *Chem. Commun.* 52 (2016) 4694–4697.
- [33] Q. Kang, T. Wang, P. Li, L.Q. Liu, K. Chang, M. Li, J.H. Ye, *Angew. Chem. Int. Ed.* 53 (2014) 1–6.
- [34] Y. Sugano, Y. Shiraishi, D. Tsukamoto, S. Ichikawa, S. Tanaka, T. Hirai, *Angew. Chem. Int. Ed.* 52 (2013) 5295–5299.
- [35] Y. Sato, S. Naya, H. Tada, *APL Mater.* 3 (2015) 104502.
- [36] A. Tanaka, K. Hashimoto, H. Kominnami, *ChemCatChem* 3 (2011) 1619–1623.
- [37] J.J. Ding, X.Y. Li, L. Chen, X. Zhang, S. Sun, J. Bao, C. Gao, X.Y. Tian, *J. Mater. Chem. A* 4 (2016) 12630–12637.
- [38] R.G. Li, F.X. Zhang, D.G. Wang, J.X. Yang, M.R. Li, J. Zhu, X. Zhou, H.X. Han, C. Li, *Nat. Commun.* 4 (2013) 1432.
- [39] C. Zhen, J.C. Yu, G. Liu, H.M. Cheng, *Chem. Commun.* 50 (2014) 10416–10419.
- [40] L. Zhang, W.Z. Wang, S.M. Sun, D. Jiang, E.P. Gao, *Appl. Catal. B Environ.* 162 (2015) 470–474.
- [41] C.Y. Dong, M.Y. Xing, J.L. Zhang, *Mater. Horiz.* 3 (2016) 608–612.
- [42] Q. Zhang, R.G. Li, Z. Li, A.L. Li, S.Y. Wang, Z.X. Liang, S.J. Liao, C. Li, *J. Catal.* 337 (2016) 36–44.
- [43] D. Wang, W.J. Wang, Q. Wang, Z.N. Guo, W.X. Yuan, *Mater. Lett.* 201 (2017) 114–117.
- [44] J.J. Ding, B. Hong, Z.L. Luo, S. Sun, J. Bao, C. Gao, *J. Phys. Chem. C* 118 (2014) 27693–27697.
- [45] H. Kato, K. Asakura, A. Kudo, *J. Am. Chem. Soc.* 125 (2003) 3082–3089.
- [46] I. Tsuji, H. Kato, H. Kobayashi, A. Kudo, *J. Am. Chem. Soc.* 126 (2004) 13406–13413.
- [47] D.W. Jing, L.J. Guo, *J. Phys. Chem. B* 110 (2006) 11139–11145.
- [48] H.F. Shi, G.Q. Chen, Z.G. Zou, *Appl. Catal. B Environ.* 156–157 (2014) 378–384.
- [49] Y. Shiraishi, H. Sakamoto, Y. Sugano, S. Ichikawa, T. Hirai, *ACS Nano* 7 (2013) 9287–9297.
- [50] S.J. Tauster, S.C. Fung, R.L. Garten, *J. Am. Chem. Soc.* 100 (1978) 170–175.
- [51] H. Tang, J. Wei, F. Liu, B. Qiao, X. Pan, L. Li, J. Liu, J. Wang, T. Zhang, *J. Am. Chem. Soc.* 138 (2016) 56–59.
- [52] S. Link, M.A. El-Sayed, *J. Phys. Chem. B* 103 (1999) 8410–8426.
- [53] J. Zhang, X.W. Xu, C. Yang, F. Yang, X.R. Yang, *Anal. Chem.* 83 (2011) 3911–3917.
- [54] J. Monzo, Y. Malewski, R. Kortlever, F.J. Vidal-Iglesias, J. Solla-Gullon, M.T.M. Koper, P. Rodriguez, *J. Mater. Chem. A* 3 (2015) 23690–23698.
- [55] M.Y. Xing, B.X. Yang, H. Yu, B.Z. Tian, S. Bagwas, J.L. Zhang, X.Q. Gong, *J. Phys. Chem. Lett.* 4 (2013) 3910–3917.
- [56] J. Hou, H. Cheng, O. Takeda, H. Zhu, *Angew. Chem. Int. Ed.* 54 (2015) 8480–8484.
- [57] A. Cybula, J.B. Priebe, M. Pohl, J.W. Sobczak, M. Schneider, A. Zielinska-Jurek, A. Bruckner, A. Zaleska, *Appl. Catal. B Environ.* 152–153 (2014) 202–211.
- [58] L. Delannoy, G. Thrimurthulu, P.S. Reddy, C. Methivier, J. Nelayah, B.M. Reddy, C. Ricolleau, C. Louis, *Phys. Chem. Chem. Phys.* 16 (2014) 26514–26527.
- [59] T.T. Jiang, C.C. Jia, L.C. Zhang, S.R. He, Y.H. Sang, H.D. Li, Y.Q. Li, X.H. Xu, H. Liu, *Nanoscale* 7 (2015) 209–217.
- [60] A. Zielinska-Jurek, E. Kowalska, J.W. Sobczak, W. Lisowski, B. Ohtani, A. Zaleska, *Appl. Catal. B Environ.* 101 (2011) 504–514.
- [61] R. Asai, H. Nemoto, Q. Jia, K. Saito, A. Iwase, A. Kudo, *Chem. Commun.* 50 (2014) 2543–2546.
- [62] B.C. Qiu, Q.H. Zhu, M.Y. Xing, J.L. Zhang, *Chem. Commun.* 53 (2017) 890–897.
- [63] N.Z. Bao, L.M. Shen, T. Takata, K. Domen, *Chem. Mater.* 20 (2008) 110–117.
- [64] C.G. Silva, R. Juarez, T. Marino, R. Molinari, H. Garcia, *J. Am. Chem. Soc.* 133 (2011) 595–602.
- [65] L. Jing, Y. Qu, B. Wang, S. Li, B. Jiang, L. Yang, W. Fu, H. Fu, J. Sun, *Sol. Energy Mater. Sol. Cells* 90 (2006) 1773–1778.
- [66] Z. Chen, L. Fang, W. Dong, F. Zheng, M. Shen, J. Wang, *J. Mater. Chem. A* 2 (2014) 824–832.
- [67] L. Sun, Y. Qi, C.J. Jia, Z. Jin, W. Fan, *Nanoscale* 6 (2014) 2649–2659.

**Fig. 11.** Schematic illustration for electron transfer mechanism in AuCu bimetallic nanoparticles under visible light irradiation.